International Journal of Environmental Science and Technology (2024) 21:6075–6092
https://doi.org/10.1007/s13762-023-05393-8

ORIGINAL PAPER

Efficient adsorption and photocatalytic degradation of textile dye from metal ion-substituted ferrite for environmental remediation

M. Sharma[1,2] · N. Mishra[3] · S. Bansal[2] · A. M. Siddiqui[1] · M. Khanuja[2]

Received: 17 March 2023 / Revised: 4 November 2023 / Accepted: 28 November 2023 / Published online: 29 December 2023

Abstract

A fuel-based solution combustion method was used to synthesize Sr-substituted copper ferrites [$Cu_{1-x}Sr_xFe_2O_4$ ($x = 0.00$, 0.25, 0.50, 0.75, 1.00)]. X-ray diffraction (XRD) pattern demonstrates that $CuFe_2O_4$ has a tetragonal structure and $SrFe_2O_4$ a cubic structure and the formation of particles of spherical and needle-like structures was observed using scanning electron microscopy (SEM). The magnetic behavior was investigated through a vibrating sample magnetometer (VSM) at room temperature under an applied magnetic field ranging from − 20 kOe to + 20 kOe. Based on the M–H hysteresis loop, the soft-ferrite nature of the samples was observed. The synthesized samples were investigated for adsorption and photocatalysis in the degradation of textile dyes malachite green, crystal violet, and congo red. Compared to other compositions, $SrFe_2O_4$ demonstrated comparatively better adsorption and photocatalytic efficiency.

Keywords Spinel ferrites · Dyes · Photocatalysis · Adsorption · Magnetic properties

Introduction

Dyes are frequently used in textile, pulp and paper, paint, food, and other industries (Affat 2021). Dyes and other industrial pollutants are highly toxic, carcinogenic, and cause environmental degradation due to their non-degradable nature (Fatima et al. 2022; Lellis et al. 2019). Pollutant reduces the reoxygenation capacity of the receiving wavelength in waterbodies due to the cutoff of sunlight that negatively influences the environment (Berradi et al. 2019). Water pollution caused by textile dyes and heavy metal ions is one of the major concerns (Ali and Gupta 2006) because they are the prime cause of dreadful diseases, and dysfunctioning of organs such as liver, brain, and kidney failure. The need for the degradation of toxic dyes from polluted water has gained appreciable attention (Jiad and Abbar 2023), particularly to develop materials that could degrade pollutants into harmless substances (Akarslan et al. 2015; Pereira et al. 2012). Depending on the nature of the contaminant, different methods are used for detoxification (Slama et al. 2021). Converting organic pollutants into harmless end products such as CO_2, water and inorganic ions through heterogeneous semiconductor oxide has become a promising technology (Rafiq et al. 2021). Several methods are used to eliminate these pollutants, e.g., adsorption, solar photo fenton method (Khaleel et al. 2023), ultrafiltration, chlorination and photocatalysis (Sharma and Kaur 2018). Every method has pros and cons; therefore, a balanced approach is needed to select a material for degrading organic pollutants. Among all, photocatalysis appears to be the most suitable method for degrading textile dyes because it is eco-friendly, provides complete degradation of pollutants, is highly efficient, and leftover products have a very low level of toxicity (Rueda-Marquez et al. 2020).

In photocatalysis, semiconducting materials are used as catalysts for dye degradation in the presence of sun-light (Mills et al. 1997). However, commonly used photocatalysts, such as TiO_2, ZnO, ZnS and MoS_2 (Khan et al. 2023), are expansive and can't be separated from the water after degradation (Jacinto et al. 2020). Filtration and centrifugation processes are commonly used to separate the photocatalyst after

Editorial responsibility: F. ŞEN.

✉ M. Khanuja
manikakhanuja@gmail.com

[1] Department of Physics, Jamia Millia Islamia, Delhi 110025, India

[2] Centre for Nanoscience and Nanotechnology, Jamia Millia Islamia, Delhi 110025, India

[3] Department of Materials Engineering, Ben-Gurion University of the Negev, 84105 Beer Sheva, Israel

the reaction. Nevertheless, these are expensive, less efficient, and time-consuming methods for separating the photocatalyst. Meanwhile, the industrial application of photocatalysts is highly restricted due to the above-mentioned problems. Therefore, photocatalyst, which possesses magnetic and photocatalytic properties, has gained significant attention (Das 2019). Consequently, spinel ferrite nanoparticles (SFNPs) have been considered a potential candidate as a photocatalyst in dye degradation to overcome the above-mentioned limitations (Ma and Liu 2021). Along with excellent photodegradation properties, these materials can easily be separated from the solution after the completion of the reaction with the help of an external magnet. Different types of SFNPs (MFe_2O_4 where M—transition metal, e.g., Co, Ni, Cu, Mn) have been extensively used as a photocatalyst due to their unique magnetic, optical, and electric properties along with thermal and chemical stability (Nie et al. 2019).

In the family of spinel ferrites, copper ferrites are extensively used in sensors, catalysis, electronics, gas sensing, hydrogen production, ceramics, and memory devices (Amiri et al. 2019). Copper ferrites possess phase transitions, interesting magnetic and electrical properties, and are non-toxic in nature (Roman et al. 2019) and it has significant potential and possesses promising outcomes in photocatalysis, reported in the previous literature (Masunga et al. 2019). The photodegradation of rhodamine B was studied using pure and Ce-doped copper ferrites (Keerthana et al. 2021). $CuFe_2O_4$@biochar composite prepared by one-step sol–gel pyrolysis method to degrade malachite green dye (Huang et al. 2021). Hydrothermally synthesized copper ferrites nanocomposite with graphene oxide was used for the malachite green degradation (Yadav et al. 2021). Photodegradation activity of TiO_2-doped copper ferrites studied toward the degradation of azo dyes (Masoumi et al. 2016). Green engineered synthesis of Ag doped copper ferrites and its catalytic activity toward malachite green degradation were investigated (Surendra 2018).

$CuFe_2O_4$ has an inverse spinel structure in which 8 Cu^{+2} ions occupy the octahedral B-site, and 16 Fe^{+3} ions occupy equal tetrahedral A-site and octahedral B-site in the unit cell (Sharma et al. 2020). This configuration can be written as $(Fe^{3+})_A[Cu^{2+}Fe^{3+}]_BO_4^{2-}$. Copper ferrites exist in two phases; cubic (stable at higher temperatures) and tetragonal (due to the Jahn–Teller distortion) (Calvo-De La Rosa and Segarra Rubí 2020). Different synthetic routes are employed to synthesize copper ferrites, such as co-precipitation, hydrothermal, solid-state, mechanical milling, electrochemical advance oxidation methods, (Jiad and Abbar 2023) thermal decomposition, microwave-assisted, and sol–gel auto combustion (Dippong et al. 2021). In the present study, the synthetic chemical route (self-propagating-combustion) was adopted due to its ease, scalability and viability in synthesizing $Cu_{(1-x)}Sr_xFe_2O_4$ nanoparticles. Citric acid monohydrate was used as a chelating agent. Furthermore, this method provides other merits, such as no post-annealing is required, high yield and good chemical homogeneity of the samples.

To the best of our knowledge, no studies till now have been carried out on the application of Sr-substituted copper ferrites for photocatalytic dye degradation and adsorption. The large ionic radius of Sr^{+2} ions as compared to Cu^{+2} ions leads to lattice distortion and hence significant alteration in material's characteristics. In a prior investigation, the addition of Sr^{+2} to cobalt ferrites resulted in a comparable effect. The study also investigates the sample's structural, optical, morphological, and magnetic characteristics and then this synthesized samples are used for the photocatalytic activity on cationic and ionic dyes as well as adsorption study are also carried out.

Materials and methods

The sol–gel auto combustion method synthesizes $Cu_{1-x}Sr_xFe_2O_4$ with x varies to 0, 0.25, 0.50, 0.75, and 1.00. $Cu(NO_3)_2{\cdot}6H_2O$, $Sr(NO_3)_2{\cdot}6H_2O$ and $Fe(NO_3)_2{\cdot}6H_2O$ of high purity (99.5%), purchased from Sigma-Aldrich, were used for sample preparation. Citric acid monohydrate was used as fuel to prepare the nanopowder. Metal nitrates and citric acid ($C_6H_8O_7{\cdot}H_2O$) were used without any further purification. Nitrate precursors were weighed stoichiometrically and mixed in 50 mL of distilled water. Subsequently, 5 g citric acid was added into the precursor's solution under continuous stirring for 15 min to mix the solution and the temperature was increased up to 90 °C, the ratio of fuel to oxidizer was 1:1. The pH of the solution was adjusted to 7 by using an ammonia solution after that solution color turns green. The ignition temperature was raised to 150 °C, and the solution covert into slurry gel under vigorous and constant stirring. The gel afterwards formed powder after the auto combustion process, and it was calcined at 700 °C, as shown in Fig. 1.

Adsorption and photocatalytic test on malachite green, crystal violet dye and congo red

Adsorption studies were carried out before the photocatalysis experiment. 20 mg of catalyst is mixed with 100 ml of dye solution. At fixed time intervals (0, 5, 10, 15, 20, 30, and 60 min), the adsorption kinetics were examined by taking 2.0 mL of the sample solution and observing for 1 h. Pseudo-first- and pseudo-second-order adsorption models were employed to study the degradation of textile dyes via adsorption. The linearized form of the kinetic model (Huang and Shih 2021) is shown in Eqs. (1 and 2).

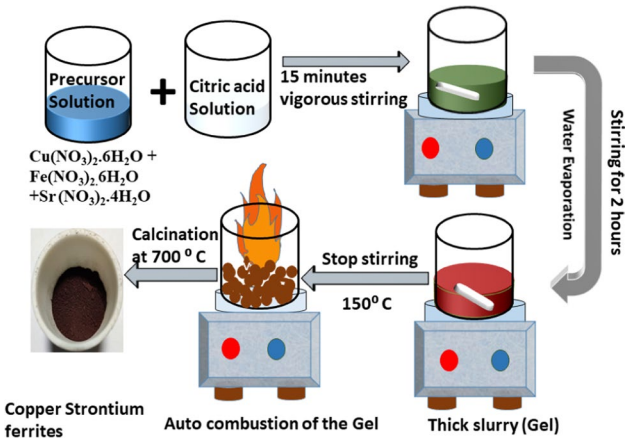

Fig. 1 Schematic of synthetic procedure for the copper strontium ferrites preparation by solution auto combustion method

$$\log\left(Q_e - Q_t\right) = \log\left(Q_e\right) - \frac{K_1}{2.303}t \tag{1}$$

$$\frac{t}{Q_t} = \frac{1}{K_2 Q_e^2} + \frac{t}{Q_e} \tag{2}$$

where K_1 and K_2 are the reaction rate constant for the first order and second order, respectively. The adsorption capacity (Q_t) can be determined from Eq. (3).

$$Q_t = \frac{(C_0 - C_t)V}{m} \tag{3}$$

where Q_t and Q_e represent adsorption capacity at time (t) and equilibrium adsorption capacity, respectively, whereas C_0 and C_t denote the initial dye concentration and dye concentration at time (t), respectively; V denotes the volume of dye solution; m stands for the mass of adsorbent.

Adsorption and photocatalysis efficiency were evaluated from Eq. (4)

$$\text{Degradation efficiency}(\%) = \left(\frac{Co - C_t}{c_0}\right) \times 100 \tag{4}$$

The photocatalytic and adsorption experiment was performed at room temperature that was around 45 °C for all the prepared samples however, we reported here for the best three catalysts ($CuFe_2O_4$, $Cu_{0.5}Sr_{0.5}Fe_2O_4$ and $SrFe_2O_4$). The adsorption and photocatalytic experiment performed individually. Initially, the adsorption experiment was performed for 60 min. Only MG was degraded in adsorption phenomenon whereas other dyes' degradation efficiency was quite less. The photocatalytic performance of $CuFe_2O_4$, $Cu_{0.5}Sr_{0.5}Fe_2O_4$ and $SrFe_2O_4$ was evaluated separately for 30 min in the degradation of textile dyes (MG, CV, and CR). The stock solution of dye was prepared, and an aliquot of stock solution was taken for photocatalysis reaction. Catalyst ($CuFe_2O_4$, $Cu_{0.5}Sr_{0.5}Fe_2O_4$ and $SrFe_2O_4$), 20 mg, was added to 100 mL of aqueous solution of dye. All the prepared solutions were exposed to sunlight for 30 min in photocatalytic reaction. At fixed time intervals, 5 ml of dye solution was pipetted out until a complete degradation of dyes. This procedure is the same for both adsorption and photocatalysis. Finally, the degradation spectra of the pollutant were observed using a UV–Vis spectrophotometer by using Eq. 4.

Characterizations

Powder XRD patterns were recorded using Rigaku Ultima IV X-ray diffractometer with a Cu $K\alpha$ source ($\lambda = 1.54$ Å) in the 2θ range 10°–80° at a rate of 2°/min). The surface morphology was examined using a high-resolution (SEM; Quanta 3D FEG). UV–Visible spectrophotometer (Agilent Technologies) was used to measure the absorption spectra at room temperature in the 200–450 nm range. The functional group of the samples has been studied from Fourier Transform infrared radiation (FTIR), Bruker tensor 37 in the range (500–4000) cm^{-1} and the Raman spectroscopy of the prepared was measured by using Invia Renishaw at 532 nm. Zeta potential measurements were done using a Malvern Zetasizer Nano ZS90, Mott–Schottky measurements were performed using potentiostat/galvanostat Autolab PGSTAT 204 (Metrohm, The Netherlands). The charge carriers' recombination times were examined by recording time-resolved photoluminescence (TRPL) using a Horiba (DeltaFlex01-DD) spectrophotometer at 280 nm excitation wavelength. The magnetic measurements were carried out at room temperature in the range of applied field −20 kOe to +20 kOe from Cryogenic Limited UK VSM.

Results and discussion

Phase analysis using X-ray diffraction

The powder XRD was used to examine the crystallinity, phase purity and crystallite size. XRD patterns of $Cu_xSr_{(1-x)}Fe_2O_4$ ($x = 0.00$, 0.25, 0.50, 0.75, and 1.00) are shown in Fig. 2. We observed the tetragonal phase of $CuFe_2O_4$ (JCPDS No. 34-0425) and cubic phase of $SrFe_2O_4$ (JCPDS No. (001-1027) in $Cu_{(1-x)}Sr_xFe_2O_4$ when $x = 0.00$ and 1.00, respectively. $SrFe_2O_4$ secondary phase was observed in $Cu_{(1-x)}Sr_xFe_2O_4$ for $x = 0.25$, 0.50, and 0.75. It confirms the substitution of Sr atoms in $CuFe_2O_4$ systems.

The presence of the $SrFe_2O_4$ phase is possibly due to phase segregation. Since the excess amount of Sr atoms occupy both substitutional and interstitial sites (tetrahedral and octahedral) in the host lattice and increases the Sr concentrations; consequently, the interaction probability increases with other atoms of the host lattice and forces them

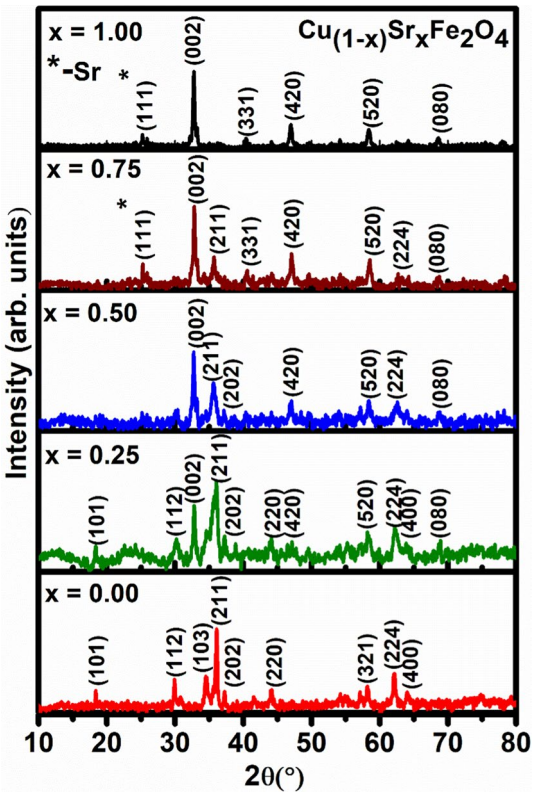

Fig. 2 XRD pattern of $Cu_{(1-x)}Sr_xFe_2O_4$ for all compositions

to leave their sites. With the higher temperature treatment given to the samples and increased Sr atoms incorporation, Gibb's free energy stabilizes and produces the secondary phase (Jelonek et al. 2020). The sharp XRD peaks indicate a high crystallinity of the as-synthesized nanocomposites.

The lattice parameters ('a' & 'c') are calculated using the interplanar spacing (d_{hkl}) given in Eq. 5.

$$\frac{1}{d_{hkl}^2} = \frac{h^2+k^2}{a^2} + \frac{l^2}{c^2} \tag{5}$$

The compositional variation of the lattice parameters is shown in Fig. 3A. Lattice parameters ('a' & 'c') are calculated taking the 2θ (hkl): 35.86° (211) and 2θ (hkl): 62.15° (224) miller plane values. The nonlinear behavior of lattice parameters indicates the contribution of both compositional and structural disorder, where the structural disorder can be attributed due to point defects. Crystallite size and the lattice strain were calculated from the line broadening of diffraction peaks of XRD using the Williamson–Hall method (Vishwaroop and Mathad 2020) and also shown in Fig. 3B. Crystallite size is also calculated using the Debye–Scherrer formula given by $D(\text{nm}) = 0.9\lambda/\beta\cos(\theta)$, where λ represents X-ray wavelength (1.5406 Å), θ is diffraction angle, and β is full-width half maximum (FWHM) (broadening of the peak) (Rabiei et al. 2020).

According to the W–H method:

$$\beta\cos\theta = \frac{k\lambda}{D} + 4\varepsilon\sin\theta \tag{6}$$

ε is the strain produced in the lattice.

A plot between $\beta\cos\theta$ and $4\sin\theta$ is shown in Fig. 4A–E. From the linear fit to the data, the strain (ε) was calculated from the slope, and the crystalline size was calculated from the y-intercept of the plot. The negative slope signifies the compressive strain in the lattice (Dey et al. 2020). The crystallite size decreases with increasing Sr concentration due to the produced lattice strain by the lattice mismatch (as given in Table 1).

Morphology study

The morphology of the synthesized $Cu_{1-x}Sr_xFe_2O_4$ nanoparticles for the selected composition was explored using SEM analysis and is shown in Fig. 5A–E. A mixed morphology, i.e., needle-like structure and spherical shape of the particles, were observed along with the large number of agglomerations suggesting the inhomogeneous synthesis process. The reason behind agglomeration is magnetic nature and primary particles union apprehended together via feeble surface interface such as van der Waals forces (Dhir et al. 2014). The uneven distribution of particles size could be due to the synthesis method.

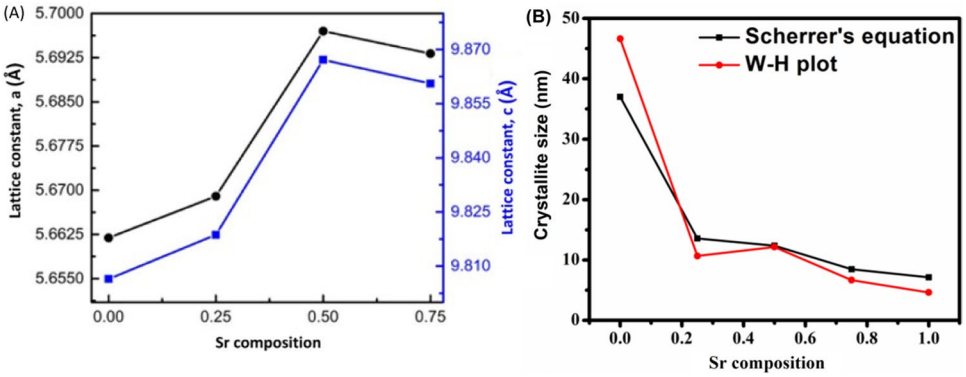

Fig. 3 Effect of Sr composition in **A** lattice parameters ('a' & 'c'), and in **B** crystallite size from Scherrer's equation and Williamson–Hall (W–H) method

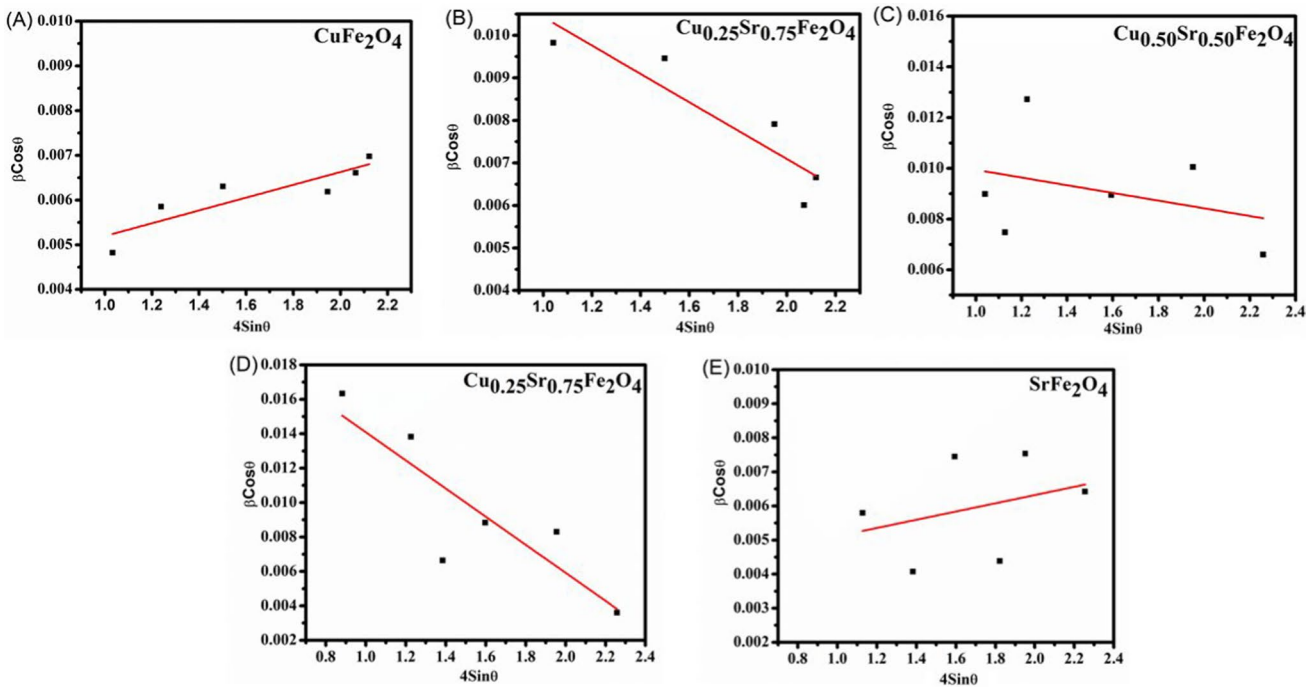

Fig. 4 Williamson–Hall (W–H) plot for $Cu_xSr_{(1-x)}Fe_2O_4$, **A** $x=0.00$, **B** $x=0.25$, **C** $x=0.50$, **D** $x=0.75$, **E** $x=1.00$

Table 1 Lattice strain and crystallite size comparison in Scherrer's method and W–H method

Samples	Crystallite size (nm) from Scherrer's equations	Crystallite size (nm) from W–H plot	Strain (ε)	Intercept
$CuFe_2O_4$	37	46.62	0.00143	0.00377
$Cu_{0.75}Sr_{0.25}Fe_2O_4$	13.56	10.66	−0.00333	0.01376
$Cu_{0.50}Sr_{0.50}Fe_2O_4$	12.36	12.15	−0.00152	0.01146
$Cu_{0.25}Sr_{0.75}Fe_2O_4$	8.45	6.66	−0.00818	0.02227
$SrFe_2O_4$	7.13	4.62	0.00121	0.00391

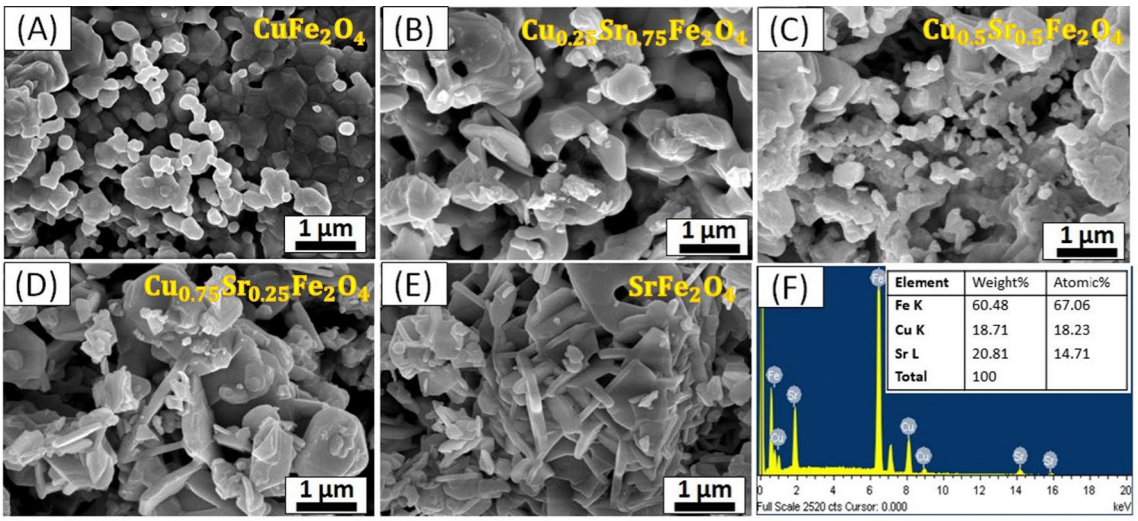

Fig. 5 SEM images of synthesized $Cu_{1-x}Sr_xFe_2O_4$ for compositions at 1 µm. **A** $x=0.00$, **B** $x=0.25$, **C** $x=0.50$, **D** $x=0.75$, **E** $x=1.00$ and **F** EDAX pattern for $Cu_{0.5}Sr_{0.5}Fe_2O_4$

UV–visible study

The absorbance spectra of undoped and Sr-doped $CuFe_2O_4$ are illustrated in Fig. 6A. The optical bandgap was estimated using Tauc's equation given by $(\alpha h\upsilon) = A\left(h\upsilon - E_g\right)^n$ where α is absorption coefficient, $h\upsilon$ is incident photon energy in eV, E_g is optical bandgap (eV), and n indicates the type of transition. For direct transition (direct bandgap), $n = 2$ is used, and for indirect transition (indirect bandgap), $n = 1/2$ is used for the bandgap estimation (Arifin et al. 2019). The E_g was estimated through the intercept, and its relationship with the compositional variation is shown in Fig. 6B. The band gap of $Cu_{(1-x)}Sr_xFe_2O_4$ was found to be decreased from 3.7 to 2.3 eV for increasing x from 0 to 1. The E_g shows a linear dependence on Sr composition x given by $E_g = 2.59 + 1.51x$ and follows ideal Vegard's law (Kempter 1966). A red shift is observed in the bandgap as the Sr composition increases, where additional sub-energy levels are introduced in the band structure due to lattice strain or point defects (Manikandan et al. 2013; Liu et al. 2004). Therefore, Sr-substituted copper ferrites can absorb more photons and generate more electrons and holes, which favors enhancing photocatalytic efficiency.

Raman and FTIR spectroscopy

According to the factor group analysis, cubic spinel has 5 Raman active mode that can be represented by $(A_{1g} + 3T_{2g} + E_g)$ and in tetragonal spinel there are 10 Raman active mode represented by $(2A_{1g} + 3B_{1g} + B_{2g} + 4E_g)$ (shown in Fig. 7A). According to the literature, the modes beyond 600 cm^{-1} (A_{1g}) frequently indicates the symmetric stretching of an oxygen atom with the metal ion at A-site. The presence of metal ions in the B-sites is responsible for the other low frequency symmetric and asymmetric bending and stretching modes (T_{2g}, B_{1g}, B_{2g}, and E_g). (Channagoudra et al. 2021).

The FTIR spectra recorded in the range (500–4000) cm^{-1} to investigate the functional group and to determine the bonding between the atoms shown in Fig. 7B, C. Two metal oxygen bonds obtained in the range (200–800) cm^{-1} one is observed at 790 cm^{-1} for metal–oxygen bond. The other one in the range (200–400) cm^{-1} was not observed because of instrument limit. The wavenumber at 3386 cm^{-1} due to the bonding of O–H. The peak that are observed in the range (3200–3700) cm^{-1} appears due to the stretching vibrations of O–H (Dhyani et al. 2022).

VSM (Vibrating sample magnetometer) measurement

The Magnetic properties of undoped and Sr-doped copper ferrites were investigated from vibrating sample magnetometer (VSM) in a magnetic field of 20 kOe. The M–H curve (Hysteresis loop) describes the material's magnetic behavior as shown in Fig. 8A–C. We calculated the saturation magnetization (M_s), Remanent magnetization (M_r), coercivity (H_c) and the squareness ratio (M_r/M_s) from the S-shaped hysteresis loop. The calculated values of M_s, M_r, H_c and squareness ratio are reported in Table 2. The value of magnetic parameters obtained from the hysteresis loop was observed to decrease with an increase in Sr-doping concentrations.

The magnetic response of the spinel ferrites depends on various parameters such as crystallite size, cation distribution in tetrahedral sites (A) and octahedral sites (B), oxygen deficiency, exchange interactions and ionic radii of alkaline earth metal (Ateia et al. 2020). In principle, there are three types of interactions in spinel ferrites, namely AOA, BOB and AOB. Interaction corresponding to the coupling of electrons with metal ions, AOB, is the strongest among them (Odio et al. 2017). $CuFe_2O_4$ belongs to the inverse spinel category, therefore, the divalent ion occupies the octahedral site, and trivalent is distributed in tetrahedral as well as octahedral sites, similar to the strontium ferrites (Ghahfarokhi and Shobegar 2020). The ionic radius of Sr^{+2} ion is larger than the Fe^{+2} ion; therefore, due to the incorporation of rare earth metals, Fe^{+2} ions migrate from the octahedral to the tetrahedral site. Consequently, AOB super exchange interaction decreases, which leads to the lower

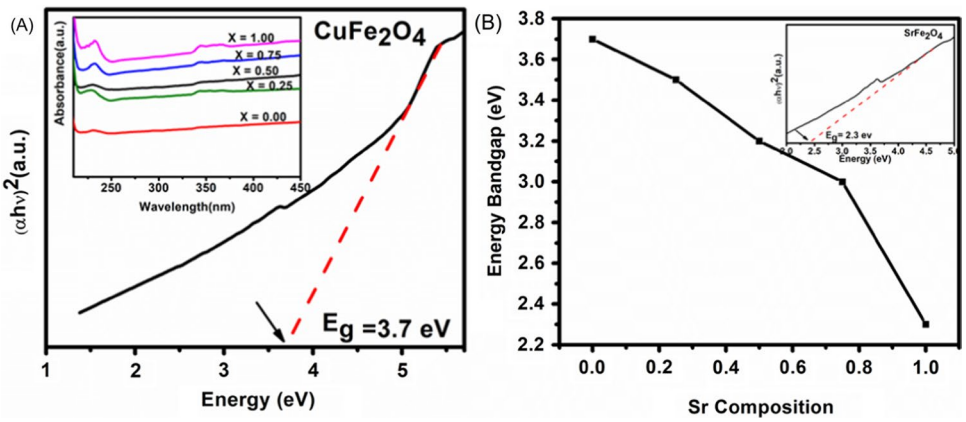

Fig. 6 **A** Tauc's plot for $CuFe_2O_4$, inserted image shows the absorption spectra of the $Cu_{1-x}Sr_xFe_2O_4$, B Variation in bandgap with Sr composition variation (inserted Tauc's plot for $SrFe_2O_4$)

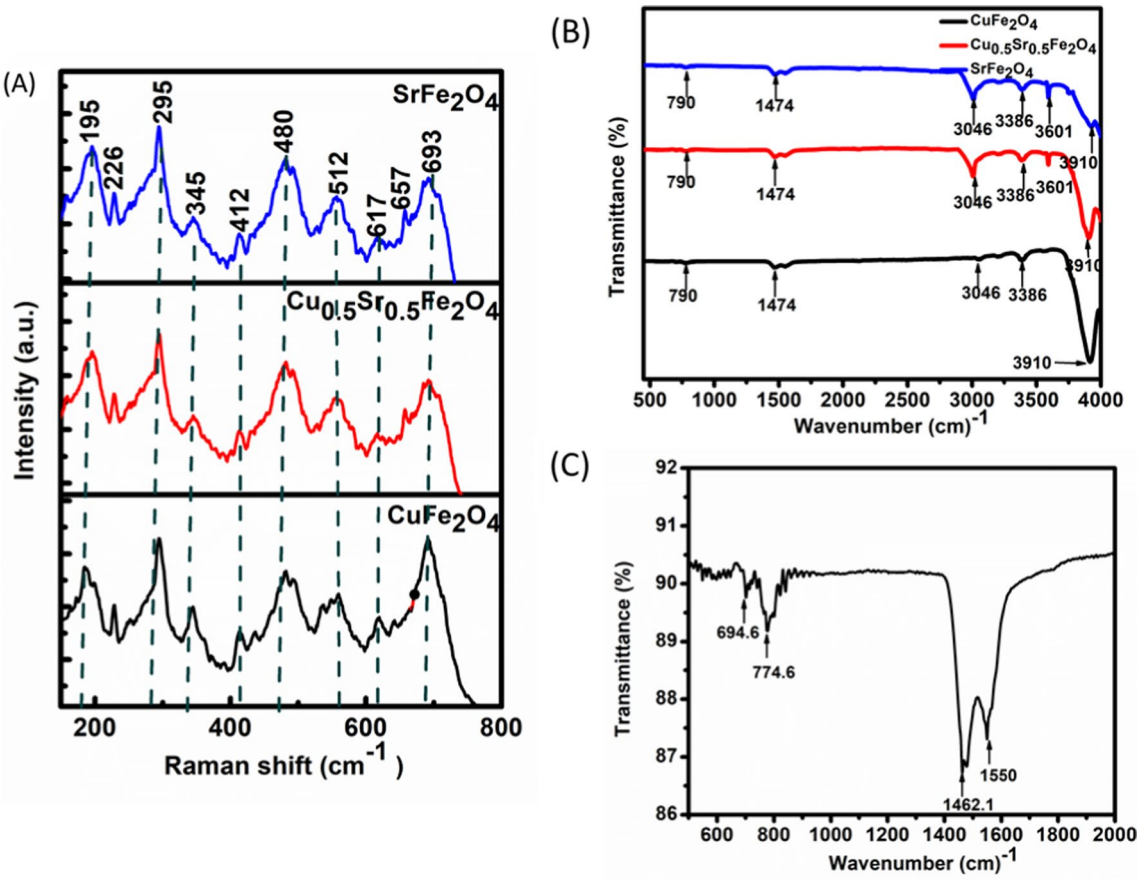

Fig. 7 **A** Raman spectra for $CuFe_2O_4$, $Cu_{0.5}Sr_{0.5}Fe_2O_4$ and $SrFe_2O_4$ and FTIR spectra for $CuFe_2O_4$, $Cu_{0.5}Sr_{0.5}Fe_2O_4$ and $SrFe_2O_4$. **C** Enlarged portion of the FTIR spectra in the range of (500–2000) cm^{-1}

value of the saturation magnetization (Abdel Maksoud et al. 2020). Another possibility for the decrement in saturation magnetization is the non-magnetic nature of Sr^{+2} ions. The synthesized samples were found to be soft ferrites due to low coercivity (see Table 2). The squareness ratio (SQR) value was observed in the range of 0.53–0.21. The materials with squareness less than 0.5 belong to the single-domain category, and those with squareness greater than 0.5 belong to the multi-domain class (Gore et al. 2022). VSM results indicate durability and easy magnetic material recovery in the applied external magnetic field.

Adsorption study

An adsorption study was performed for MG, CV and CR dyes; however, only MG was degraded significantly and the rest of the dyes degraded below 55%. The possible reason for the difference in efficiencies is due to the small structural change in MG and CV. There are different factors such as charge density, electron distribution, substitutions present or steric factors which may responsible for this difference in efficiencies in cationic and anionic dyes (Liu et al. 2004; Zhuo et al. 2011). The adsorption experiment was done in the dark for one hour, and MG was observed to be degraded maximum from the Uv–Vis spectrometer. C/C_0 vs time plotted for dark degradation as shown in Fig. 9A. Efficiency was calculated and obtained to be 68% in copper ferrites (SF1), 82% in copper strontium ferrites (SF2) and 92% in strontium ferrites (SF3) (shown in Fig. 9B).

Adsorption kinetics

To investigate the reaction mechanism of the adsorption of dye on the surface of the catalyst, two kinetic models, first and second order, were considered. Adsorption plots for first- and second-order kinetics are shown in Fig. 10A, B. The values of rate constants K_1 and K_2, corresponding linear regression coefficient (R^2), were calculated and shown in Table 3. A lower R^2 value for first-order reaction, reveals that the first-order model does not predict the rate kinetics of adsorption of MG dye on the nanocomposite surface. However, the R^2 value corresponding to second-order kinetics is close to 1 and indicates that second-order model is suitable for the adsorption of MG onto the catalyst surface.

Therefore, we conclude that the adsorption of MG follows pseudo-second-order kinetic model and chemisorption is paramount in the adsorption reaction (Sahoo et al. 2018; Vergis et al. 2018).

Adsorption mechanism

In principle, the adsorption mechanism contains three main steps (Alaqarbeh 2021).

1. Film diffusion, where adsorbate ions or molecules transfer from the bulk solution to the external surface of the adsorbent's particles due to the boundary layer.
2. Intraparticle diffusion, where the adsorbate transports into adsorbent either due to the internal pores (pore diffusion) or through the internal surface (surface diffusion).
3. Energetic interaction between the final adsorbate and internal adsorption active sites (Worch 2012; Han et al. 2017).

The adsorption process rate, in general, is controlled by the second and third steps, whereas the first step occurs rapidly.

The adsorbent initially encounters the solution of adsorbate material then the pores of the adsorbent's material are filled with water (pores water). In the first step of adsorption process, the metal ion transforms from a bulk solution to a thin film solution and surrounds the adsorbent by a layer which is known as the boundary layer. The concentration of the adsorbate (dye molecules) in the solution decreases because the adsorbent ion (catalyst) ensnared into the boundary layer. This film diffusion process is the rate-governing mechanism in the adsorption process until the adsorbate concentration equilibrates in the bulk and boundary layer solutions.

More reduction of the adsorbate concentration in the bulk solution depends on intraparticle diffusion of adsorbate ions/molecules through pore diffusion and/or surface diffusion (Han et al. 2017). This reduction in concentration can be explained by Weber-Morris intraparticle diffusion model.

$$q_t = kt^{0.5} + c \tag{7}$$

where q refers to the solid phase concentration (mg/g), i.e., quantity of adsorbate on the adsorbent, t is the adsorption time (minutes), k is the rate constant (mg/g–$h^{0.5}$) for film or intraparticle diffusion, and c is a proportionality constant for the boundary layer thickness (mg/g). If the intraparticle diffusion is the solitary rate-controlling mechanism, then the q versus $t^{0.5}$ gives a straight line that passes through the origin. A non-zero intercept means another mechanism is also involved in the adsorption process (Singh et al. 2012).

Two intraparticle diffusion rate constants have been calculated from the linear fit data. The adsorption mechanism can be explained based on the above explanation. The steep slope K_1 represents the rapid adsorption process due to the electrostatic interaction between the adsorbate and adsorbent. K_1 was found to be maximum for $SrFe_2O_4$ and correlated with maximum degradation efficiency. The value of the first slope is larger than the second one, see Fig. 10C. The second slope K_2 is more gradual, representing a slow diffusing process (Mortazavian et al. 2019).

The adsorption efficiency is maximum for $SrFe_2O_4$, and adsorption isotherms at different concentrations (1 mg/100 ml, 2 mg/100 ml, 3 mg/100 ml and 4 mg/100 ml) were studied for $SrFe_2O_4$. The Langmuir and Freundlich adsorption isotherms were used to investigate the adsorption capability of MG at different equilibrium concentrations.

Table 2 Magnetic parameters obtained from VSM measurements

Samples	M_s (emu/g)	M_r (emu/g)	H_c (Oe)	SQR (M_r/M_s)
$CuFe_2O_4$	23.18	12.5	1520	0.53
$Cu_{0.5}Sr_{0.5}Fe_2O_4$	18.22	8.92	820	0.48
$SrFe_2O_4$	8.78	1.86	260	0.21

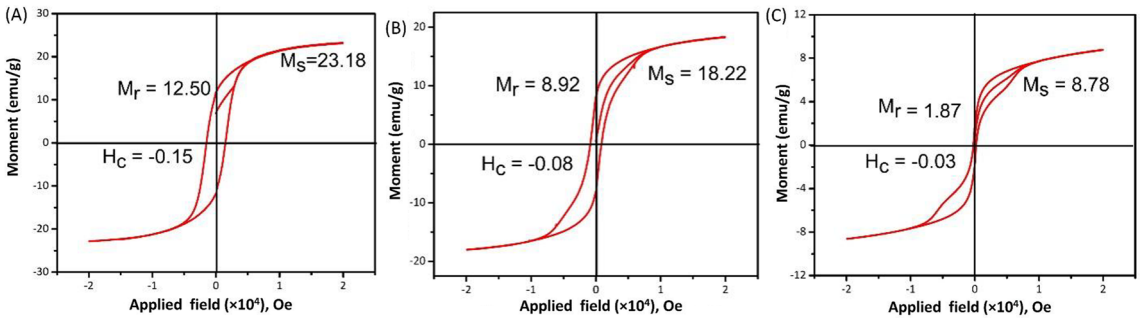

Fig. 8 VSM plot of **A** $CuFe_2O_4$, **B** $Cu_{0.5}Sr_{0.5}Fe_2O_4$ and **C** $SrFe_2O_4$

$$\frac{C_e}{q_e} = \frac{1}{k_L Q_m} + \frac{C_e}{Q_m} \tag{8}$$

$$\log\left(q_e\right) = \log\left(k_f\right) + \frac{1}{n}\log\left(C_e\right) \tag{9}$$

The amount of dye adsorbed at the equilibrium concentration is q_e, C_e is the concentration of solute at equilibrium, maximum adsorption capacity is Q_m and K_L is the equilibrium constant of Langmuir isotherms. K_f and $1/n$ are the Freundlich constants related to adsorption intensity and adsorption capacity, respectively (Edet and Ifelebuegu 2020; Chen 2015). Figure 10D, E shows the fitting results for the isotherms Langmuir and Freundlich adsorption model. Isotherm constants obtained from the fitted data are given in Table 4. We obtained Langmuir isotherm adsorption model is better fit for adsorption equilibrium of Malachite Green on $CuFe_2O_4$, $Cu_{0.5}Sr_{0.5}Fe_2O_4$ and $SrFe_2O_4$. In Langmuir model, one dye molecule is adsorbed on an individual (one) adsorption site, and a monolayer is formed on the surface of the adsorbent, resulting decrease in the adsorption sites for further layer (Alaqarbeh 2021). The half life of the photocatalyst was also calculated from the below expression (Mahmoud et al. 2009)

$$t_{1/2} = \frac{0.693}{k} \tag{10}$$

We have calculated the half life of the photocatalyst from rate constant. The minimum decrement in half life is obtained in diffusion model and second-order rate kinetics. We have calculated the half life of the photocatalyst from rate constant. The minimum decrement in half life is obtained in diffusion model and second-order rate kinetics (as given in Table 3).

The feasibility and favorability of adsorption are determined by Langmuir dimensionless separation factor R_L shown in Eq. (10).

$$R_L = \frac{1}{1+k_L C_0} \tag{11}$$

R_L value lies in the range (0–1) favors the adsorption process, whereas $R_L > 1$ indicates the unfavorable adsorption (Ayawei et al. 2017). R_L value obtained from Langmuir isotherms is 0.92 and confirms the favorable adsorption (as given in Table 5).

Adsorption isotherms was studied for $Cu_{0.5}Sr_{0.5}Fe_2O_4$ and found that it is also follows Langmuir isotherms model as the $SrFe_2O_4$ followed.

Effect of pH and temperature on degradation of dye

The effect of temperature has been studied at three different temperature 30 °C, 50 °C and 70 °C from $SrFe_2O_4$ (SF3) for 30 min in case of adsorption. Increase in temperature leads to improved dye adhesion on catalyst surfaces compared to lower temperatures. As indicated in Fig. 11A, the adsorption efficiency varies with temperature. When the temperature increased from 303 to 343 K, there was an initial increase in adsorption efficiency from 75 to 95% for a 1 mg/100 ml concentration at pH 7.0. This observation suggests that the adsorption reaction is endothermic in nature. (Karthikeyan et al. 2005) The enhanced adsorption efficiency at higher temperatures may be attributed to chemical interactions between adsorbates and the adsorbent, potentially resulting in the creation of additional adsorption sites or an accelerated rate of pollutant ion diffusion into the pores of the adsorbent.

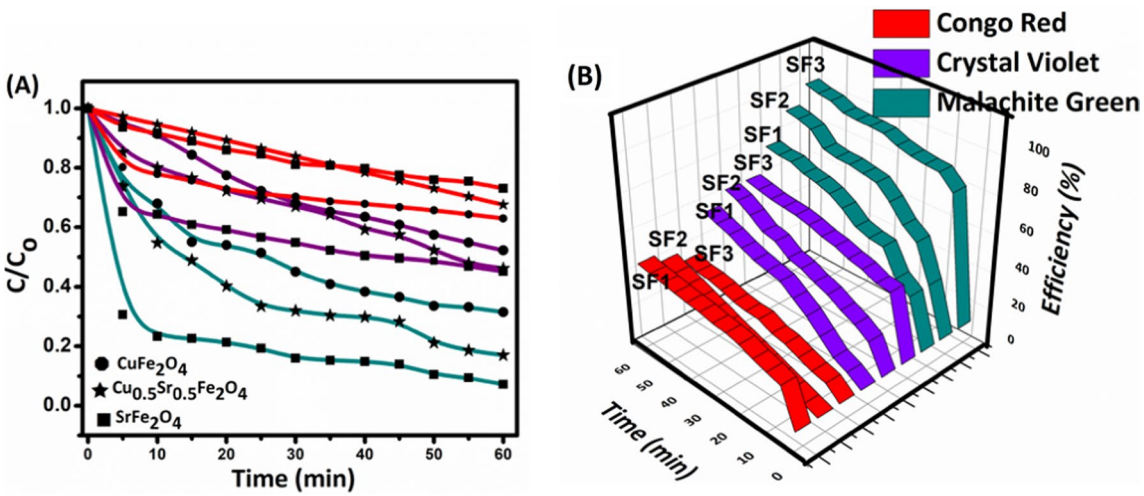

Fig. 9 **A** C/Co plot for dark degradation. **B** Efficiency plot in case of malachite green, crystal violet and congo red for $CuFe_2O_4$ (SF1), $Cu_{0.5}Sr_{0.5}Fe_2O_4$ (SF2) and $SrFe_2O_4$ (SF3)

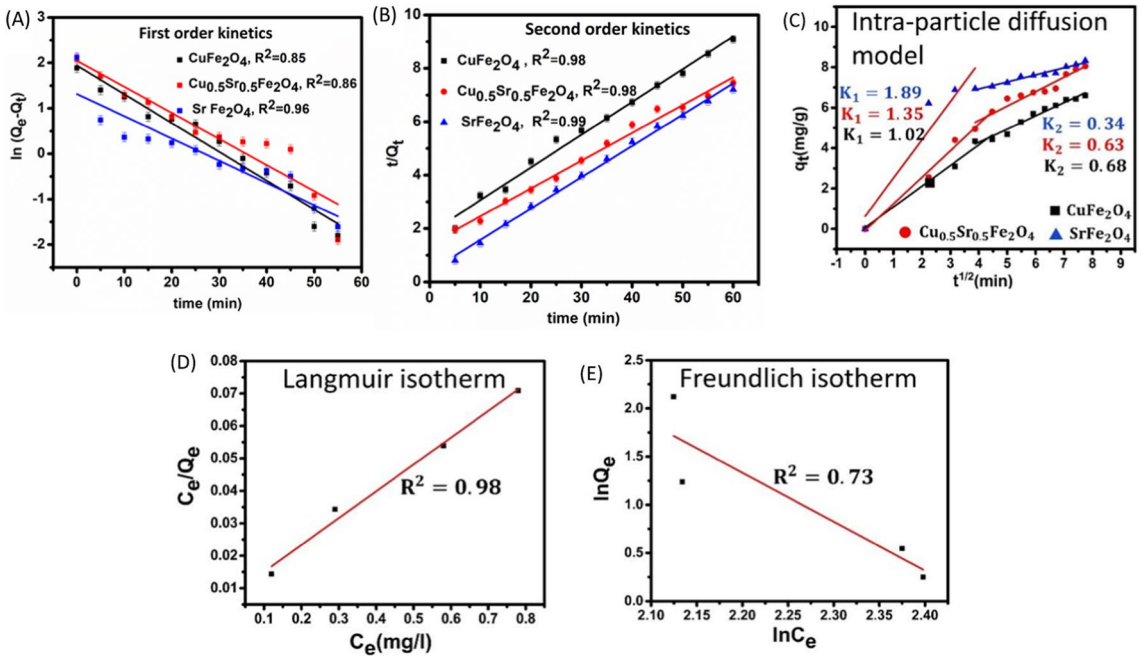

Fig. 10 The adsorption mechanism model for malachite green **A** the first-order kinetics model; **B** the second-order kinetics model; **C** diffusion model langmuir isotherm model; **D** langmuir isotherm model; **E** Freundlich isotherm model

Table 3 Kinetic model parameters from fitted data

Samples	$CuFe_2O_4$	$Cu_{0.5}Sr_{0.5}Fe_2O_4$	$SrFe_2O_4$
(a) First-order model K_1(g/mg/min)	0.04	0.05	0.06
(b) Half life (min^{-1})	17.32	13.86	11.55
(c) Second-order model K_2(g/mg/min)	0.12	0.11	0.10
(d) Half life (min^{-1})	5.77	6.30	6.93
(e) Diffusion model K_1($min^{1/2}$·g·mg^{-1})	1.02	1.35	1.89
(f) Half life (min^{-1})	0.67	0.51	0.36
K_2($min^{1/2}$·g·mg^{-1})	0.68	0.63	0.34
(g) Half life (min^{-1})	1.01	1.10	2.03

K_1: first-order slope, K_2: second-order slope, R^2: correlation coefficient

Effect of pH Usually, the pH of the solution plays a very crucial role in wastewater treatment, and it is a very important factor that influence the photocatalytic degradation process of organic compounds. The effect of pH on the degradation of MG was studied at pH values of 4, 7 and 9 and it was found that efficiency increases as pH vary from (4–9), i.e., the photodegradation efficiency increases from acidic to alkaline medium (Rahman et al. 2021) (shown in Fig. 11 B. This result indicates that the photodegradation process occurs at the catalyst surface and not in bulk solution. In addition, one would expect that the interaction between the photogenerated holes and hydroxide ions (OH) to generate hydroxyl radicals (OH) is enhanced in alkaline pH, which in turn would facilitate the photocatalytic degradation of MG. The maximum degradation efficiency was obtained 95.04% at pH 9. The increased proton concentration in acidic solutions slows down the dye's photodegradation, which lowers the degradation efficiency. In a basic Conversely, the existence of the acidic end products are neutralized by hydroxyl ions once they are generated by the process of photodegradation.

Photocatalytic degradation of textile dyes (malachite green, crystal violet, congo red)

The photocatalytic activities of $CuFe_2O_4$, $Cu_{0.5}Sr_{0.5}Fe_2O_4$ and $SrFe_2O_4$ nanocomposite were evaluated by degrading malachite green, crystal violet and congo red dyes. We found that complete degradation of MG occurred in 30 min. The catalyst $SrFe_2O_4$ displayed the highest photodegradation efficiency due to uniform structure and negative surface charge. The photo-decolorization of MG was found to 93.20% for

copper ferrite, 94.50% for Cu–Sr ferrites and 97.00% for strontium ferrites. For CV, 16.92% efficiency was observed in the presence of $CuFe_2O_4$, and 26.15% dye was degraded by $Cu_{0.5}Sr_{0.5}Fe_2O_4$ photocatalyst, while 41.67% degradation was observed for $SrFe_2O_4$. Notably, the surface charge of $SrFe_2O_4$ is negative and supports cation dye degradation. Therefore, from Fig. 12A, B, it can be concluded that $SrFe_2O_4$ exhibits relatively better photocatalytic activity compared to pure copper ferrites and their composites.

The photocatalytic degradation efficiency of CR in the presence of CuFe2O4, $Cu_{0.5}Sr_{0.5}Fe_2O_4$ and $SrFe_2O_4$ nanocomposite is shown in Fig. 12B. It was observed that after 30 min, about 83.64% of CR was degraded in the presence of $CuFe_2O_4$, and 73.03% was degraded by $Cu_{0.5}Sr_{0.5}Fe_2O_4$ photocatalyst, while 72.98% degradation was observed for $SrFe_2O_4$. Photocatalysis efficiency is minimal for $SrFe_2O_4$ due to the interaction between the anionic dye and the negatively charged surface of $SrFe_2O_4$. Moreover, photocatalytic efficiency was enhanced in light compared to dark in half time.

Zeta potential and TRPL (time-resolved photoluminescence) studies

Zeta potential study was performed to investigate the surface charge of $CuFe_2O_4$, $Cu_{0.5}Sr_{0.5}Fe_2O_4$ and $SrFe_2O_4$. The $CuFe_2O_4$ and $Cu_{0.5}Sr_{0.5}Fe_2O_4$ exhibited a positive zeta potential of + 5.49 mV and + 3.08 mV, respectively, while $SrFe_2O_4$ showed a negative zeta potential of − 13.8 mV (see Fig. 13A. These results are in good agreement with the previous literature (Kamel et al. 2020). We calculated the surface charge for $Cu_{0.75}Sr_{0.25}Fe_2O_4$ and $Cu_{0.25}Sr_{0.75}Fe_2O_4$ nanocomposites, and their values were obtained to be + 4.42 mV and − 1.21 mV, respectively. Sr-doped $CuFe_2O_4$ samples suggest the higher dispersion stability of nanoparticles in the solution. The opposite surface charge favors the adsorption of cationic dye (malachite green and crystal violet) on the $SrFe_2O_4$ photocatalyst due to the electrostatic force of attraction. Degradation efficiency is observed less for anionic dye (congo red) because of the opposite surface charge.

The enlarged portion of decay-associated spectra of Sr-substituted Cu ferrites is shown in Fig. 13B. However, the complete decay spectra of the samples are shown in the inset Fig. 13B. The calculation and fitting of the experimental data were implemented by triexponential function using Eq. 12 (Chen et al. 2012).

$$y = A_1 + B_1 e\left(-\frac{i}{\tau_1}\right) + B_2 e\left(\frac{-i}{\tau_2}\right) + B_3 e\left(\frac{-i}{\tau_3}\right) \quad (12)$$

where B_1, B_2 and B_3 are amplitudes, τ_1, τ_2, and τ_3 correspond to the lifetime of components 1, 2 and 3, respectively. The average lifetime of the samples $CuFe_2O_4$, $Cu_{0.5}Sr_{0.5}Fe_2O_4$ and $SrFe_2O_4$ were found to be 2.07 ns, 3.62 ns and 3.90 ns, respectively. The recombination time was obtained maximum for $SrFe_2O_4$, which can be correlated with the higher degradation efficiency. The χ^2 value was obtained in the good fit data range. The TRPL results (see Table 7) of undoped and Sr-doped copper ferrites indicated high charge carrier recombination in Sr ferrite, which correlates with better photocatalytic performance (Table 6).

Table 4 Isotherms model constants describing the adsorption of Malachite green on $SrFe_2O_4$

Langmuir isotherms	$SrFe_2O_4$	Freundlich isotherms	$SrFe_2O_4$
Q_m (mg/g)	1000	K_f ($mg^{1-1/n}.L^{1/n}.g^{-1}$)	280
K_L (L/g)	0.082	n	3.98
R_L	0.92	R^2	0.78
R^2	0.98		

Q_m: maximum adsorption capacity, K_L: Langmuir equilibrium constant, R_L: separation factor, R_2: correlation coefficient, K_f and n: Freundlich constants

Mott Schottky measurement

Mott Schottky measurements were conducted in 0.1 M solution ofNa_2SO_4 with Ag/AgCl electrode for $CuFe_2O_4$, $Cu_{0.5}Sr_{0.5}Fe_2O_4$ and $SrFe_2O_4$ nanocomposites. We calculated the flat band potential and the positions of the valance band (VB) and conduction band (CB) (see Fig. 14A-C). The negative slope demonstrates that $CuFe_2O_4$, $Cu_{0.5}Sr_{0.5}Fe_2O_4$ and $SrFe_2O_4$ possess a p-type conductivity. These results are in good agreement with the previous literature (Fedailaine et al. 2016). The flat band potential value for $CuFe_2O_4$, $Cu_{0.5}Sr_{0.5}Fe_2O_4$ and $SrFe_2O_4$ nanocomposites are − 0.28 V, − 0.09 V and − 0.84 V, respectively (see Table 8).

Reported degradation efficiencies of textile dyes on photocatalysts

Here, we collected the reported degradation efficiencies of the textile dyes due to photocatalysts in Table 9. We compare our results with the reported data on the degradation of textile dyes using copper ferrites and their composites in Table 9. The comparison is made on the basis of the degradation efficiency and performance of the synthesized samples. The present work shows better degradation efficiency of MG, CV and CR dyes using Sr-substituted copper ferrites (97%, 41.67% and 72.98%, respectively) and consumed relatively lesser time to degrade the dyes (see Table 9).

Mechanism of textile dye de-colorization

The photocatalytic degradation mechanism of textile dyes is shown in Fig. 15. When the surface of photocatalyst

($CuFe_2O_4$, $Cu_{0.5}Sr_{0.5}Fe_2O_4$ and $SrFe_2O_4$) is irradiated by UV–vis light, electrons in the valance band get excited, as shown in Eq. 13. Furthermore, the complete mechanisms of photodegradation are shown in Eqs. 13–21. Electrons jump to the conduction band and create an equal number of holes in the valance band (Ajormal et al. 2020). The holes in the VB can directly react with dye or interact with water and form hydroxyl radicals (·OH), a powerful oxidant for the mineralization of dyes. Meanwhile, the photogenerated electron can be captured by absorbed reactive oxygen molecules to yield O_2^-. The generated O_2^- reacts with H^+ to produce H_2O_2, which further reacts with the excited electrons and generates OH^- radicals. All the reactive radicals react with the dye and lead to the formation of degradation products. Sr-substituted copper ferrites have a lower band gap than pure copper ferrites. $CuFe_2O_4$ band gap was determined from Tauc's plot as 3.7 eV, which lies in the UV–Vis region, i.e., ~ 5% of the solar spectrum. However, the modified bandgap of Sr-substituted copper ferrites (2.3 eV) lies in the visible region (which is approx. 46% of the spectrum) that enhances the photocatalytic degradation efficiency of the synthesized material.

$$SeFe_2O_4 + h\nu \rightarrow SrFe_2O_4(e^-) + SrFe_2O_4\left(h^+\right) \quad (13)$$

$$SrFe_2O_4(e^-) + O_2 \rightarrow .O_2^- \quad (14)$$

$$H_2O \rightleftharpoons H^+ + OH^- \quad (15)$$

$$OH^- + h_{VB}^+ \rightarrow .OH \quad (16)$$

Table 5 Isotherms model constants describing the adsorption of Malachite green on $SrFe_2O_4$

Langmuir isotherms	$Cu_{0.5}Sr_{0.5}Fe_2O_4$	Freundlich isotherms	$Cu_{0.5}Sr_{0.5}Fe_2O_4$
Q_m(mg/g)	700	K_f ($mg^{1-1/n}.L^{1/n}.g^{-1}$)	250
K_L(L/g)	0.078	n	3.16
R_L	0.92	R^2	0.77
R^2	0.96		

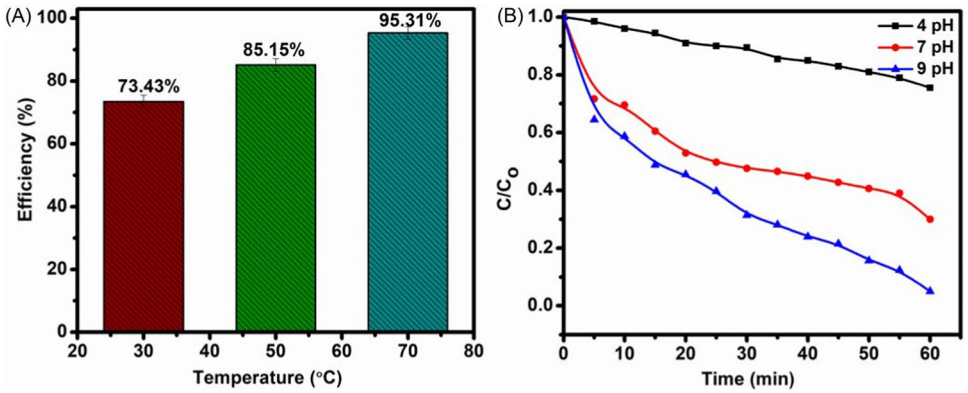

Fig. 11 **A** Effect of temperature on MG dye degradation, **B** effect of pH on degradation of dye MG from $SrFe_2O_4$ (SF3)

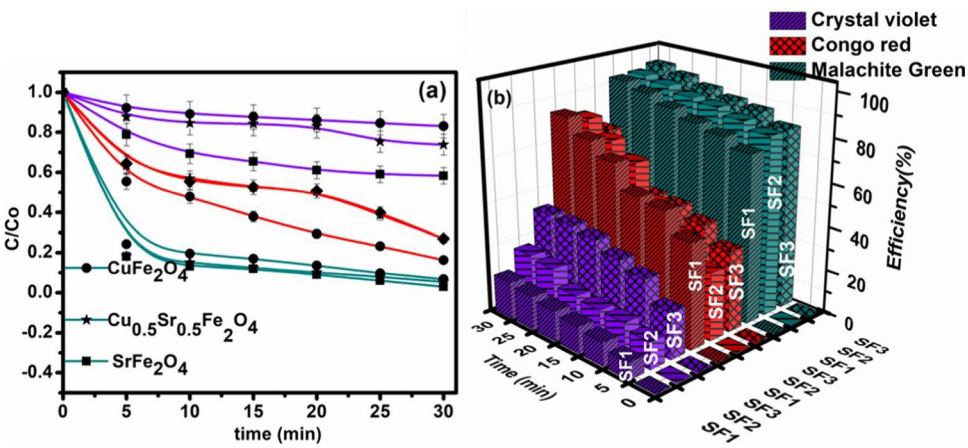

Fig. 12 Photocatalysis degradation of textile dyes (MG, CV, and CR) for $CuFe_2O_4$ (SF1), $Cu_{0.5}Sr_{0.5}Fe_2O_4$ (SF2) and $SrFe_2O_4$ (SF3), **A** C/Co plot **B** efficiency with time (min)

$$SeFe_2O_4(e^-) + .O_2^- + 2H^+ \rightarrow H_2O_2 \quad (17)$$

$$SeFe_2O_4(e^-) + H_2O_2 \rightarrow .OH + OH^- \quad (18)$$

$$SrFe_2O_4(h^+) + H_2O \rightarrow .OH + H^+ \quad (19)$$

$$MG + .OH \rightarrow \text{Degradation Products} \quad (20)$$

$$MG + .O_2^- \rightarrow \text{Degradation Products} \quad (21)$$

Scavenger test for malachite green (MG)

To investigate the role of the active species, including holes (h^+), hydroxyl radicals (·OH) and superoxide radicals ($\cdot O_2$) which are responsible for the degradation of dyes, trapping experiments were performed in the representative dye MG. Different types of scavengers were used for trapping active species. Radicals benzoquinone (BQ) was used for the superoxide, KI for holes and hydroxyl radicals trapping; however, t-BuOH for hydroxyl radicals (Janani et al. 2021). As expected, it was observed that maximum photodegradation efficiency was obtained without a scavenger. However, photodegradation efficiency with the scavenger decreased due to the trapping of produced active species by the scavenger (see Fig. 16). The photocatalytic degradation efficiency for malachite green is reduced to 73.8% from 98.8% (blank, i.e., without scavenger) after the addition of BQ, implying that superoxide radicals are mainly responsible for the degradation of MG. The degradation efficiency was reduced to 96.8% with KI; however, the degradation efficiency remains unchanged for t-BuOH (see Fig. 16). Based on the scavenger test, it is observed that superoxide radicals ($\cdot O_2$) and hydroxyl radicals (·OH) are the major and minor active species for the degradation of MG, respectively. Similarly, the scavenger test can be performed for the other dyes as well. In addition, H_2O_2 was also used as scavenger in scavenger test. H_2O_2 generates super oxide and hydroxyl radical that are responsible to degrade the pollutant. The degradation efficiency is 91% in case of H_2O_2.

The reusability of the magnetic photocatalyst

The reusability of a catalyst plays a crucial role in using it for industrial applications. We tested reusability for the strontium ferrites, and 20 mg of the photocatalyst was used in 100 ml of dye solution. After the photodegradation process, the photocatalyst was magnetically extracted using a magnet. To remove the remnant dye molecule on strontium ferrite, the used strontium ferrites were washed thrice with 10 ml of ethanol followed by 10 ml of deionized water. The difference in colour of MG dye is shown in Fig 17A. The recyclability was tested five times to verify the reusability of strontium ferrite, and obtained efficiencies were 97%, 96%, 95%, 93% and 92%, respectively, shown in Fig. 17B. There is a slight change in degradation efficiency, which confirms the reusability of the photocatalyst.

Table 6 The degradation efficiency of all synthesized samples

Samples	Degradation efficiency (η)		
	MG (cationic dye) (%)	CV (cationic dye) (%)	CR (anionic dye) (%)
$CuFe_2O_4$	93.20	16.92	83.64
$Cu_{0.5}Sr_{0.5}Fe_2O_4$	94.50	26.15	73.03
$SrFe_2O_4$	97.00	41.67	72.98

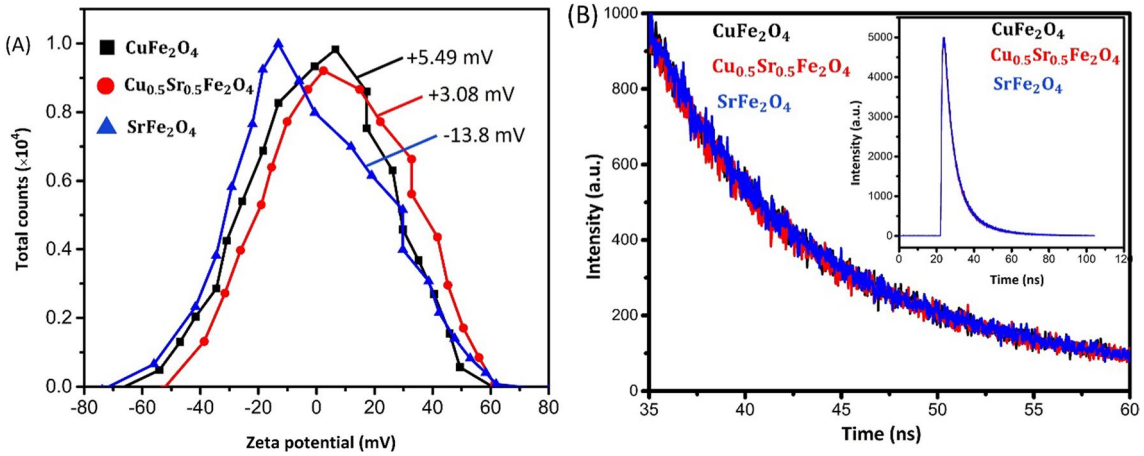

Fig. 13 **A** Zeta potential and **B** time-resolved photoluminescence (TRPL) for samples $CuFe_2O_4$, $Cu_{0.5}Sr_{0.5}Fe_2O_4$ and $SrFe_2O_4$

Table 7 TRPL data of undoped and Sr-doped copper ferrites

Sample	Lifetime (ns)			Relative amplitude (%)			Average lifetime (ns)	χ^2
	τ_1	τ_2	τ_3	B_1	B_2	B_3	τ	
$CuFe_2O_4$	3.83	11.64	0.23	41.50%	50.73%	7.77%	2.07	1.10
$Cu_{0.5}Sr_{0.5}Fe_2O_4$	4.23	12.39	0.58	45.83%	46.61%	7.57%	3.62	1.11
$SrFe_2O_4$	4.20	12.24	0.62	45.33%	47.80%	6.87%	3.90	1.06

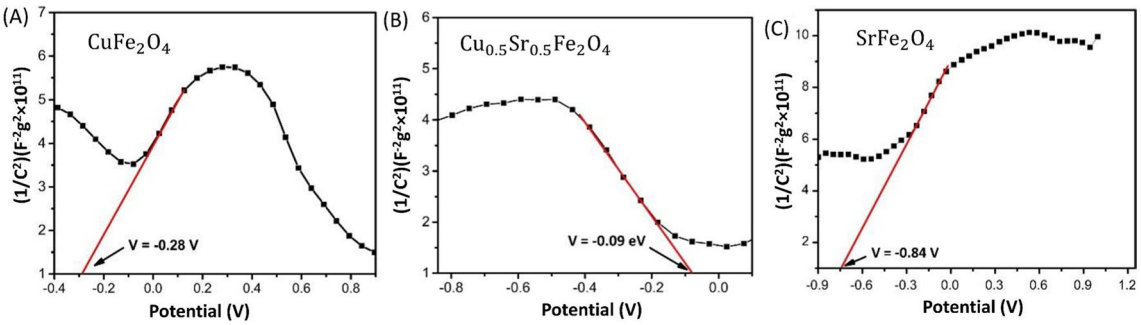

Fig. 14 **A** Mott Schottky plot for $CuFe_2O_4$, **B** $Cu_{0.5}Sr_{0.5}Fe_2O_4$ and **C** $SrFe_2O_4$

Table 8 Mott–Schottky measurements of synthesized samples

Sample	Position of conduction band	Position of valance band	Flat band position (V)	Bandgap (eV)
$CuFe_2O_4$	−0.377	+3.32	−0.28	3.7
$Cu_{0.5}Sr_{0.5}Fe_2O_4$	−0.187	+3.01	−0.09	3.2
$SrFe_2O_4$	−0.70	+1.36	−0.84	2.3

Table 9 Reports on copper ferrites and their composites for degradation of different dyes

Photocatalyst	Light source	Amount of catalyst (mg)	Pollutant	Degradation efficiency (%)	Time (minutes)	Reference
$CuFe_2O_4$	Visible	20	Malachite green Rhodamine B	56 84	60	Oliveira et al. (2022)
$Ag@CuFe_2O_4$	UV–Vis	30	Malachite green	97	240	Surendra (2018)
$CuFe_2O_4$@ Biochar composites	Visible	100	Malachite green	98.9	80	Huang et al. (2021)
$Ce@CuFe_2O_4$	Visible	100	Rhodamine B	88	120	Keerthana et al. (2021)
$SrFe_2O_4/g\text{-}C_3N_4$	Visible	50	Rhodamine B	93.4	40	Bo et al. (2019)
AFe_2O_4 (A = Ba, Ca and Sr)	Xenon lamp	100	Congo red	92.72 84.65 80.05	75	Vijayaraghavana et al. (2016)
$GO/CuFe_2O_4$	Visible	10	Malachite green	90.7	240	(Yadav et al. 2021)
$CuFe_2O_4/AgBr$	Visible	50	Methyl orange Tetracycline hydrochloride	91.1 89.1	160	Zhao et al. (2017)
$Cu_{1-x}Ni_xFe_2O_4$	Visible	310	Rhodamine B	99.6	300	(Dhiwahar et al. 2021)
$CuFe_2O_4–TiO_2$	UV–Vis	100	Congo red	99	60	Masoumi et al. (2016)
$Cu_{1-x}Sr_xFe_2O_4$	Visible	20	Malachite green Crystal violet Congo red	97 41.67 72.98	30	Present work

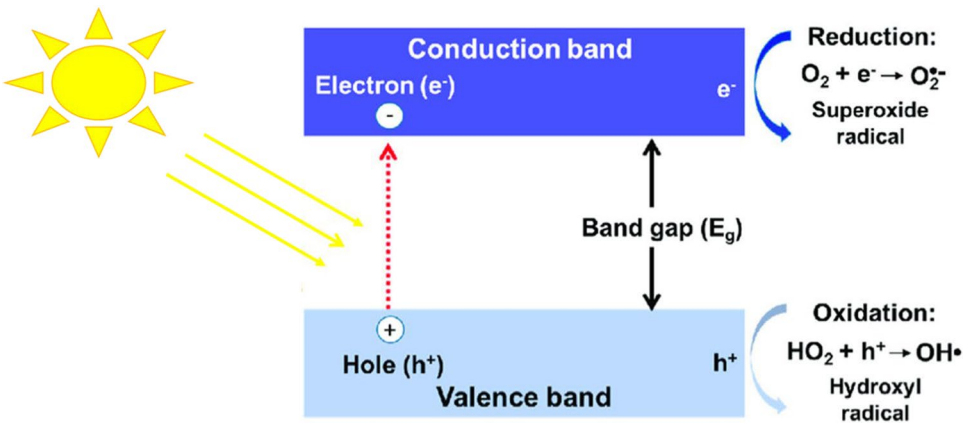

Fig. 15 Schematic to explain photocatalysis mechanism

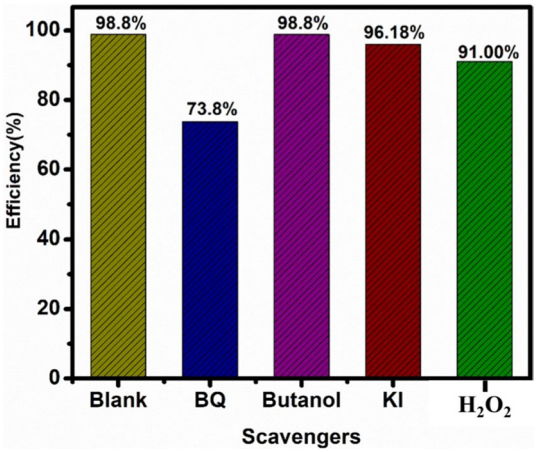

Fig. 16 Scavenger test using $SrFe_2O_4$ for Malachite green

Conclusion

$Cu_{1-x}Sr_xFe_2O_4$ (where x varies from 0 to 1) were synthesized using a fuel-based sol–gel auto-combustion method. The X-ray diffraction pattern indicated the formation of different structures, including a single-phase tetragonal spinel for $CuFe_2O_4$ ($x=0$), a cubic spinel for $SrFe_2O_4$ ($x=1$). The particles exhibited mixed morphologies, with both spherical and needle-like shapes observed. The optical bandgap decreased from 3.7 eV ($x=0$) to 2.3 eV ($x=1$). The adsorption and photocatalytic properties of the prepared samples were studied for dye degradation. Maximum adsorption was observed for MG, and the highest decolorization efficiency, reaching 97%, was achieved for $SrFe_2O_4$. Photocatalytic degradation efficiency improved under light compared to dark conditions in half time. The adsorption mechanism followed

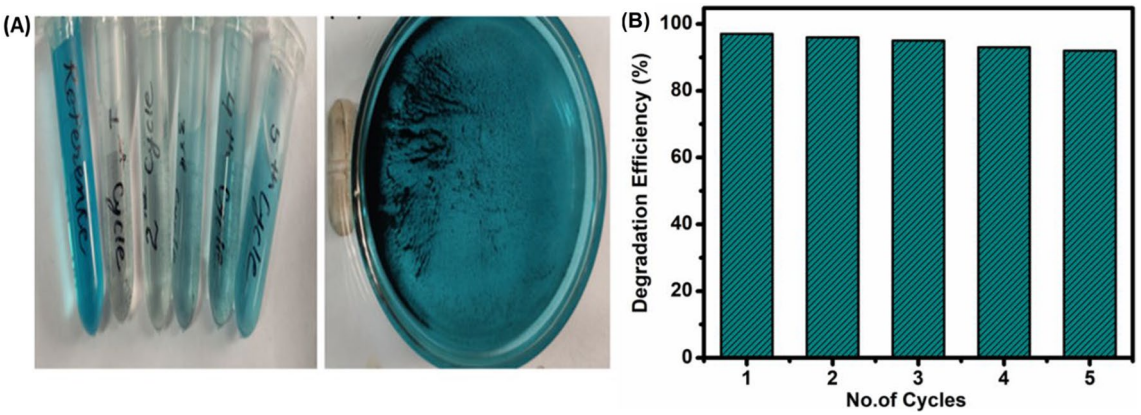

Fig. 17 **A** Color difference in MG dye in the presence of photocatalyst with a digital photograph of recovery of magnetic photocatalyst from dye solution **B** degradation efficiency for five cycles

the second-order kinetic model and intra-particle diffusion model, consistent with Langmuir isotherms. For various dyes, the highest photocatalytic efficiency was achieved with strontium ferrites (97% for MG, 41.67% for CV, and 72.98% for CR), except for copper ferrites, which achieved 83.64% efficiency in CR degradation. The magnetic study showed that samples exhibited a ferromagnetic nature. This property allowed for easy recovery and magnetic separation of the nanocatalysts from the reaction mixture. Consequently, these highly efficient and reusable photocatalysts offer a promising solution for the degradation of industrial pollutants. The photocatalyst was found to be reusable for up to five cycles, especially in the case of $SrFe_2O_4$.

Acknowledgements We acknowledge the Central Instrumentation Facility Centre and Center for nanoscience and nanotechnology, Jamia Millia Islamia (JMI) and AIRF (JNU) for their help with the characterization facilities. The presented work was supported by (Dr. Manika Khanuja), SERB, [ECR/2017/001222] Nanomission, (DST) [DST/NM/NB/2018/203(G)(JMI)].

Author contributions MS: data curation, formal analysis, methodology, software, writing—original draft, conceptualization, investigation, validation, visualization, writing—review & editing. NM: conceptualization, validation, visualization, writing—review & editing. SB: validation. AMS: supervision, validation, writing—review & editing. MK: funding acquisition, project administration, resources, supervision, conceptualization, writing—review & editing.

Funding Support of the Department of Science and Technology vide [DST/NM/NB/2018/203(G)(JMI)] is highly acknowledged.

Data availability The datasets generated during and/or analyzed during the current study are available from the corresponding author on reasonable request.

Declarations

Conflict of interest Authors declare no conflicts of interest.

Ethical approval This is an observational study, and the research ethics committee has confirmed that no ethical approval is required.

Consent to participate All individual participants are included in the study. Please keep this consent form in the patient's case files. The manuscript reporting this patient's details should state that 'Written informed consent for publication of their clinical details and/or clinical images' was obtained from the patient/parent/guardian/ relative of the patient. A copy of the consent form is available for review by the Editor of this journal.

References

Abdel Maksoud MIA, El-Sayyad GS, Abd Elkodous M, Awed AS (2020) Controllable synthesis of $Co_{1-x}M_xFe_2O_4$ Nanoparticles (M=Zn, Cu, and Mn; x = 0.0 and 0.5) by cost-effective sol–gel approach: analysis of structure, elastic, thermal, and magnetic properties. J Mater Sci Mater Electron 31(12):9726–9741. https://doi.org/10.1007/s10854-020-03518-0

Abdulla Y, Abbar AH (2023) Applications of advanced oxidation processes (Electro-Fenton and sono-electro-Fenton) for COD removal from hospital wastewater: optimization using response surface methodology. Process Saf Environ Prot 169(2023):481–492. https://doi.org/10.1007/s13399-021-01753-x

Affat SS (2021) Classifications, advantages, disadvantages, toxicity effects of natural and synthetic dyes: a review. UTJ Sci 8(1):130–135

Ajormal F, Moradnia F, Taghavi Fardood S, Ramazani A (2020) Zinc ferrite nanoparticles in photo-degradation of dye: mini-review. J Chem Rev 2(2):90–102. https://doi.org/10.33945/sami/jcr.2020.2.2

Akarslan F, Demiralay H (2015) Effects of textile materials harmful to human health. Acta Phys Polonica A 128(2):407–408. https://doi.org/10.12693/APhysPolA.128.B-407

Alaqarbeh M (2021) Adsorption phenomena: definition, mechanisms, and adsorption types short review. RHAZES Green Appl Chem 13:43–51. https://doi.org/10.48419/IMIST.PRSM/rhazes-v13.28283

Ali I, Gupta VK (2006) Advances in water treatment by adsorption technology. Nature Protoc 1(6):2661–2667. https://doi.org/10.1038/nprot.2006.370

Amiri M, Eskandari K, Salavati-Niasari M (2019) Magnetically retrievable ferrite nanoparticles in the catalysis application. Adv Coll Interface Sci 271:101982. https://doi.org/10.1016/j.cis.2019.07.003

Arifin MN, Karim KMR, Abdullah H, Khan MR (2019) Synthesis of titania doped copper ferrite photocatalyst and its photoactivity towards methylene blue degradation under visible light irradiation. Bull Chem React Eng Catal 14(1):219–227. https://doi.org/10.9767/bcrec.14.1.3616.219-227

Ateia EE, Abdelmaksoud MK, Arman MM, Shafaay AS (2020) Comparative study on the physical properties of rare-earth-substituted nano-sized $CoFe_2O_4$. Appl Phys A Mater Sci Process 126(2):1–10. https://doi.org/10.1007/s00339-020-3282-5

Ayawei N, Ebelegi AN, Wankasi D (2017) Modelling and interpretation of adsorption isotherms. J Chem. https://doi.org/10.1155/2017/3039817

Berradi M, Hsissou R, Khudhair M, Assouag M, Cherkaoui O, El Bachiri A, El Harfi A (2019) Textile finishing dyes and their impact on aquatic environs. Heliyon. https://doi.org/10.1016/j.heliyon.2019.e02711

Bo L, Yusen Hu, Zhang Z, Tong J (2019) Efficient photocatalytic degradation of rhodamine B catalyzed by $SrFe_2O_4$/g-C_3N_4 composite under visible light. Polyhedron 168:94–100. https://doi.org/10.1016/j.poly.2019.04.036

Calvo-de la Rosa J, Segarra Rubí M (2020) Influence of the synthesis route in obtaining the cubic or tetragonal copper ferrite phases. Inorg Chem 59(13):8775–8788. https://doi.org/10.1021/acs.inorgchem.0c00416

Channagoudra G, Saw AK, Dayal V (2021) Role of structure and cation distribution on magnetic and electrical properties in inverse spinel copper ferrite. J Phys Chem Solids 154:110086. https://doi.org/10.1016/j.jpcs.2021.110086

Chen X (2015) Modeling of experimental adsorption isotherm data. Information (switzerland) 6(1):14–22. https://doi.org/10.3390/info6010014

Chen YC, Pu YC, Hsu YJ (2012) Interfacial charge carrier dynamics of the three-component in $2O_3$–TiO_2–Pt heterojunction system. J Phys Chem C 116(4):2967–2975. https://doi.org/10.1021/jp210033y

Das S (2016) Research progress on iron oxide-based magnetic materials: synthesis techniques and photocatalytic applications. Remote Sens Appl Soc Environ 42(1):9–34. https://doi.org/10.1016/j.rsase.2019.02.006

Dey PC, Sarkar S, Das R (2020) X-ray diffraction study of the elastic properties of jagged spherical CdS nanocrystals. Mater Sci Poland 38(2):271–278. https://doi.org/10.2478/msp-2020-0032

Dhir G, Uniyal P, Verma NK (2014) Effect of particle size on multiferroism of barium-doped bismuth ferrite nanoparticles. Mater Sci Semicond Process 27:611–618. https://doi.org/10.1016/j.mssp.2014.07.041

Dhiwahar AT, Maruthamuthu S, Marnadu R, Sundararajan M, Manthrammel MA, Shkir M, Sakthivel P, Reddy VRM (2021) Improved photocatalytic degradation of rhodamine B under visible light and magnetic properties using microwave combustion grown ni doped copper ferrite spinel nanoparticles. Solid State Sci 113:106542. https://doi.org/10.1016/j.solidstatesciences.2021.106542

Dhyani R et al (2022) Structural and elastic properties of tetragonal nano-structured copper ferrite. Int J Mater Res 113(10):884–892. https://doi.org/10.1515/ijmr

Dippong T, Levei EA, Cadar O (2021) Recent advances in synthesis and applications of MFe_2O_4 (M=Co, Cu, Mn, Ni, Zn) nanoparticles. Nanomaterials 11(6):3–8. https://doi.org/10.3390/nano11061560

Edet UA, Ifelebuegu AO (2020) Kinetics, isotherms, and thermodynamic modeling of the adsorption of phosphates from model wastewater using recycled brick waste. Processes 8(6):665. https://doi.org/10.3390/PR8060665

Fatima T, Husain S, Khanuja M (2022) Superior photocatalytic and electrochemical activity of novel WS2/PANI nanocomposite for the degradation and detection of pollutants: antibiotic, heavy metal ions, and dyes. Chem Eng J Adv 12(July):100373. https://doi.org/10.1016/j.ceja.2022.100373

Fedailaine M, Bellal B, Berkani S, Trari M, Abdi A (2016) Photo-electrochemical characterization of the spinel $CuFe_2O_4$: application to Ni2+ removal under solar light. Environ Process 3(2):387–396. https://doi.org/10.1007/s40710-016-0142-6

Ghahfarokhi SEM, Shobegar EM (2020) Influence of PH on the structural, magnetic and optical properties of $SrFe_2O_4$ nanoparticles. J Mater Res Technol 9(6):12177–12186. https://doi.org/10.1016/j.jmrt.2020.08.063

Gore SK, Tumberphale UB, Jadhav SS, Shaikh SF, Al-Enizi AM, Rana AUHS, Khule RN, Raut SD, Gore TS, Mane RS (2022) Grain and grain boundaries influenced magnetic and dielectric properties of lanthanum-doped copper cadmium ferrites. J Mater Sci Mater Electron 33(10):7636–7647. https://doi.org/10.1007/s10854-022-07912-8

Han S, Liu K, Linfeng Hu, Teng F, Pingping Yu, Zhu Y (2017) Superior adsorption and regenerable dye adsorbent based on flower-like molybdenum disulfide nanostructure. Sci Rep 7(January):1–11. https://doi.org/10.1038/srep43599

Huang Y-T, Shih M-C (2021) Application of the analysis toolpak for comparison of various linearized expressions of kinetics equations for sorption of methylene blue onto nitric acid-treated rice husk. Int J Sci Res Publ (IJSRP) 11(6):692–698. https://doi.org/10.29322/ijsrp.11.06.2021.p11490

Huang Q, Chen C, Zhao X, Bu X, Liao X, Fan H, Gao W, Hu H, Zhang Y, Huang Z (2021) Malachite green degradation by persulfate activation with $CuFe_2O_4$@biochar composite: efficiency, stability and mechanism. J Environ Chem Eng 9(4):105800. https://doi.org/10.1016/j.jece.2021.105800

Jacinto MJ, Ferreira LF, Silva VC (2020) Magnetic materials for photocatalytic applications—a review. J Sol Gel Sci Technol 96(1):1–14. https://doi.org/10.1007/s10971-020-05333-9

Janani B, Syed A, Thomas AM, Al-Rashed S, Elgorban AM, Raju LL, Khan SS (2021) A simple approach for the synthesis of bifunctional p-n type ZnO@$CuFe_2O_4$ heterojunction nanocomposite for photocatalytic and antimicrobial application. Phys E Low Dimens Syst Nanostruct 130:114664. https://doi.org/10.1016/j.physe.2021.114664

Jelonek Z, Drobniak A, Mastalerz M, Jelonek I (2020) Environmental implications of the quality of charcoal briquettes and lump charcoal used for grilling. Sci Total Environ 747:141267. https://doi.org/10.1016/j.scitotenv.2020.141267

Jiad MM, Abbar AH (2023) Treatment of petroleum refinery wastewater by electrofenton process using a low cost porous graphite air-diffusion cathode with a novel design. Chem Eng Res Des 193:207–221

Kamel AH, Hassan AA, Amr AEGE, El-Shalakany HH, Al-Omar M (2020) Synthesis and characterization of $CuFe_2O_4$ nanoparticles modified with polythiophene: applications to mercuric ions removal. Nanomaterials 10(3):586. https://doi.org/10.3390/nano10030586

Karthikeyan T, Rajgopal S, Miranda LR (2005) Chromium (VI) adsorption from aqueous solution by *Hevea Brasilinesis* sawdust activated carbon. J Hazard Mater 124(1–3):192–199

Keerthana SP, Yuvakkumar R, Ravi G, Pavithra S, Thambidurai M, Dang C, Velauthapillai D (2021) Pure and Ce-doped spinel $CuFe_2O_4$ photocatalysts for efficient rhodamine B degradation. Environ Res. https://doi.org/10.1016/j.envres.2021.111528

Kempter CP (1966) Vegard's 'Law.' Phys Status Solidi b 18(2):K117–K118. https://doi.org/10.1002/pssb.19660180251

Khaleel GF, Ismail I, Abbar AH (2023) Application of solar photo-electro-Fenton technology to petroleum refinery wastewater degradation: optimization of operational parameters. Heliyon 9(4):e15062

Khan M et al (2023) Investigation of the annealing temperature for few-layer MoS2 and ion-beam induced athermal annealing/purification behaviour by in-situ XRD. Appl Surface Sci 639:158106

Lellis B, Fávaro-Polonio CZ, Pamphile JA, Polonio JC (2019) Effects of textile dyes on health and the environment and bioremediation potential of living organisms. Biotechnol Res Innov 3(2):275–290. https://doi.org/10.1016/j.biori.2019.09.001

Liu W, Chao Y, Yang X, Bao H, Qian S (2004) Biodecolorization of Azo, anthraquinonic and triphenylmethane dyes by white-rot fungi and a laccase-secreting engineered strain. J Ind Microbiol Biotechnol 31(3):127–132. https://doi.org/10.1007/s10295-004-0123-z

Ma H, Liu C (2021) A mini-review of ferrites-based photocatalyst on application of hydrogen production. Front Energy 15(3):621–630. https://doi.org/10.1007/s11708-021-0761-0

Mahmoud MA, Poncheri A, Badr Y, Abd El Wahed MG (2009) Photocatalytic degradation of methyl red dye. South Afr J Sci 105(7):299–303

Manikandan A, Judith Vijaya J, Sundararajan M (2013) Optical and magnetic properties of Mg-doped $ZnFe_2O_4$ nanoparticles prepared by rapid microwave combustion method. Superlattices Microstruct 64(1):118–131. https://doi.org/10.1016/j.spmi.2013.09.021

Masoumi S, Nabiyouni G, Ghanbari D (2016) Photo-degradation of azo dyes: photo catalyst and magnetic investigation of $CuFe_2O_4$–TiO_2 nanoparticles and nanocomposites. J Mater Sci Mater Electron 27(9):9962–9975. https://doi.org/10.1007/s10854-016-5067-3

Masunga N, Mmelesi OK, Kebede KK, Mamba BB (2019) Recent advances in copper ferrite nanoparticles and nanocomposites synthesis, magnetic properties and application in water treatment: review. J Environ Chem Eng 7(3):103179. https://doi.org/10.1016/j.jece.2019.103179

Mills A, Le Hunte S (1997) An overview of semiconductor photocatalysis. J Photochem Photobiol, A 108(1):1–35. https://doi.org/10.1016/S1010-6030(97)00118-4

Mortazavian S, Saber A, Hong J, Bae JH, Chun D, Wong N, Gerrity D, Batista J, Kim KJ, Moon J (2019) Synthesis, characterization, and kinetic study of activated carbon modified by polysulfide rubber coating for aqueous hexavalent chromium removal. J Ind Eng Chem 69:196–210. https://doi.org/10.1016/j.jiec.2018.09.028

Nie J, Sun Y, Zhou Y, Kumar M (2019) Bioremediation of water containing pesticides by microalgae: mechanisms, methods, and prospects for future research. Sci Total Environ 707:136080. https://doi.org/10.1016/j.scitotenv.2019.136080

Odio OF, Reguera E (2017). Nanostructured spinel ferrites: synthesis, functionalization, nanomagnetism and environmental applications. In: Magnetic spinels—synthesis, properties and applications, pp 185–216, https://doi.org/10.5772/67513

Oliveira TP, Rodrigues SF, Marques GN, Viana Costa RC, Garçone Lopes CG et al (2022) Synthesis, characterization, and photocatalytic investigation of $CuFe_2O_4$ for the degradation of dyes under visible light. Catalysts 12:623

Pereira L, Alves M (2012) Dyes-environmental impact and remediation. Environ Prot Strateg Sust Dev. https://doi.org/10.1007/978-94-007-1591-2_4

Rabiei M, Palevicius A, Monshi A, Nasiri S, Vilkauskas A, Janusas G (2020) Comparing methods for calculating nano crystal size of natural hydroxyapatite using X-Ray diffraction. Nanomaterials 10(9):1–21. https://doi.org/10.3390/nano10091627

Rafiq A, Muhammad Ikram S, Ali FN, Khan M, Khan Q, Maqbool M (2021) Photocatalytic degradation of dyes using semiconductor photocatalysts to clean industrial water pollution. J Ind Eng Chem 97:111–128. https://doi.org/10.1016/j.jiec.2021.02.017

Rahman MU et al (2021) Solar driven photocatalytic degradation potential of novel graphitic carbon nitride based nano zerovalent iron doped bismuth ferrite ternary composite. Opt Mater 120:111408

Roman T, Pui A, Lukacs AV, Cimpoesu N, Lupescu S, Borhan AI, Kordatos K et al (2019) Structural changes of cerium doped copper ferrites during sintering process and magneto-electrical properties assessment. Ceram Int 45(14):17243–17251. https://doi.org/10.1016/j.ceramint.2019.05.280

Rueda-Marquez JJ, Levchuk I, Ibañez PF, Sillanpää M (2020) A critical review on application of photocatalysis for toxicity reduction of real wastewaters. J Clean Prod 258:120694. https://doi.org/10.1016/j.jclepro.2020.120694

Sahoo JK, Kumar A, Rout L, Rath J, Dash P, Sahoo H (2018) An investigation of heavy metal adsorption by hexa-dentate ligand-modified magnetic nanocomposites. Sep Sci Technol 53(6):863–876. https://doi.org/10.1080/01496395.2017.1406950

Sharma M, Singh AK, Siddiqui AM (2020) Synthesis and characterization of copper ferrite nanoparticles. In: AIP conference proceedings, vol 2265, p 030170. https://doi.org/10.1088/1757-899X/928/7/072125

Sharma S, Kaur A (2018) Various methods for removal of dyes from industrial effluents—a review. Indian J Sci Technol 11(12):1–21. https://doi.org/10.17485/ijst/2018/v11i12/120847

Singh SK, Townsend TG, Mazyck D, Boyer TH (2012) Equilibrium and intra-particle diffusion of stabilized landfill leachate onto micro- and meso-porous activated carbon. Water Res 46(2):491–499. https://doi.org/10.1016/j.watres.2011.11.007

Slama HB, Bouket AC, Pourhassan Z, Alenezi FN, Silini A, Cherif-Silini H, Oszako T, Luptakova L, Golińska P, Belbahri L (2021) Diversity of synthetic dyes from textile industries, discharge impacts and treatment methods. Appl Sci (switzerland) 11(14):1–21. https://doi.org/10.3390/app11146255

Surendra BS (2018) Green engineered synthesis of ag-doped $CuFe_2O_4$: characterization, cyclic voltammetry and photocatalytic studies. J Sci Adv Mater Devices 3(1):44–50. https://doi.org/10.1016/j.jsamd.2018.01.005

Vergis BR, Hari Krishna R, Nagaraju Kottam BM, Nagabhushana RS, Darukaprasad B (2018) Removal of malachite green from aqueous solution by magnetic $CuFe_2O_4$ nano-adsorbent synthesized by one pot solution combustion method. J Nanostruct Chem 8(1):1–12. https://doi.org/10.1007/s40097-017-0249-y

Vijayaraghavana T, Suriyarajb SP, Selvakumarb R, Venkateswarana R, Ashoka A (2016) Rapid and efficient visible light photocatalytic dye degradation using AFe_2O_4 (A = Ba, Ca and Sr) complex oxides 3. Mater Sci Eng B 1(1):1–11. https://doi.org/10.1016/j.mseb.2016.04.005

Vishwaroop R, Mathad SN (2020) Synthesis, structural, W–H plot and size-strain analysis of nano cobalt doped Mgfe2o4 Ferrite. Sci Sinter 52(3):349–358. https://doi.org/10.2298/SOS2003349V

Worch E (2012) Adsorption technology in water treatment. De Gruyter, Berlin. ttps://doi.org/10.1515/9783110240238

Yadav P, Surolia PK, Vaya D (2021) Synthesis and application of copper ferrite-graphene oxide nanocomposite photocatalyst for the degradation of malachite green. Mater Today Proc 43:2949–2953. https://doi.org/10.1016/j.matpr.2021.01.301

Zhao Y, Lin C, Bi H, Liu Y, Yan Q (2017) Magnetically separable $CuFe_2O_4$/AgBr composite photocatalysts: preparation, characterization, photocatalytic activity and photocatalytic mechanism under visible light. Appl Surf Sci 392:701–707. https://doi.org/10.1016/j.apsusc.2016.09.099

Zhuo R, Ma Li, Fan F, Gong Y, Wan X, Jiang M, Zhang X, Yang Y (2011) Decolorization of different dyes by a newly isolated white-rot fungi strain *Ganoderma* sp.En3 and cloning and functional analysis of its laccase gene. J Hazard Mater 192(2):855–873. https://doi.org/10.1016/j.jhazmat.2011.05.106